

# Broadband merged-element Josephson parametric amplifier

Yuting Sun,<sup>1,2,3,a)</sup> Xianke Li,<sup>1,2,3</sup> Qingyu Wang,<sup>1,2</sup> Tairong Bai,<sup>1,2,3</sup> Xudong Liao,<sup>1,2</sup> Dong Lan,<sup>1,2,3,4</sup> Jie Zhao,<sup>1,2,3,b)</sup> and Yang Yu<sup>1,2,3,4</sup>

<sup>1)</sup>National Laboratory of Solid State Microstructures, School of Physics, Nanjing University, Nanjing 210093, China

<sup>2)</sup>Shishan Laboratory, Suzhou Campus of Nanjing University, Suzhou 215163, China

<sup>3)</sup>Hefei National Laboratory, Hefei 230088, China

<sup>4)</sup>Synergetic Innovation Center of Quantum Information and Quantum Physics, University of Science and Technology of China, Hefei, Anhui 230026, China

(Dated: June 6 2025)

Broadband quantum-limited amplifiers are essential for quantum information processing, yet challenges in design and fabrication continue to hinder their widespread applications. Here, we introduce the broadband merged-element Josephson parametric amplifier in which the discrete parallel capacitor is directly integrated with the Josephson junctions. This merged-element design eliminates the shortcomings of discrete capacitors, simplifying the fabrication process, reducing the need for high-precision lithography tools, and ensuring compatibility with standard superconducting qubit fabrication procedures. Experimental results demonstrate a gain of 15 dB over a 500 MHz bandwidth, a mean saturation power of -116 dBm and near-quantum-limited noise performance. This robust readily implemented parametric amplifier holds significant promise for broader applications in superconducting quantum information and the advancement of quantum computation.

Quantum limited parametric amplifiers are essential for quantum information and quantum metrology processes<sup>1-4</sup>. In superconducting quantum information, a quantum-limited Josephson parametric amplifier (JPA)<sup>5-7</sup> is typically used as the preamplifier to suppress the readout noise and enhance the signal-to-noise ratio (SNR). Josephson parametric amplifiers are key components for realizing high-fidelity single-shot readout<sup>8,9</sup>, generating squeezed quantum states<sup>10,11</sup>, implementing weak measurements<sup>12-14</sup>, performing real-time quantum feedback<sup>15</sup>, and achieving quantum error correction (QEC)<sup>16-18</sup>.

In the Noisy Intermediate-Scale Quantum (NISQ) era, a broadband parametric amplifier is necessary to fulfill the requirement of instantaneous readout of multiple qubits. Based on this requirement, a variety types of broadband Josephson parametric amplifiers have been proposed and experimentally demonstrated. They can be generally categorized into two types: the impedance-transformed parametric amplifier (IMPA)<sup>19-29</sup>, and the traveling wave parametric amplifier (TWPA)<sup>30-34</sup>. Although TWPAs are capable of achieving bandwidths greater than 1 GHz, their fabrication process is comparatively more complex. Furthermore, their gain profile is often insufficiently flat, and their ultra-wide bandwidth is frequently limited by other cryogenic microwave devices in the system. IMPAs are commonly used in superconducting quantum information experiments owing to their balance between gain, bandwidth, and fabrication compatibility<sup>27</sup>.

Lumped capacitors in parallel with the Josephson junctions play a crucial role in achieving simultaneously high gain and broad bandwidth in IMPAs. Various types of capacitors have been employed in IMPAs, such as interdigital capacitors<sup>22</sup>, vacuum gap capacitors<sup>26</sup>, and dielectric parallel-plate capacitors<sup>21,23</sup>. Each type of capacitor has its own shortcomings.

The parasitic inductance of an interdigital capacitor is inevitable and limits the working frequency range of a parametric amplifier<sup>26</sup>. The yield of vacuum gap capacitors is hard to improve, and the stability of vacuum gap capacitors is generally inferior to that of other types capacitors. Dielectric parallel-plate capacitors normally require multi-layer fabrication processes, and imperfections in the dielectric layer can lead to defects and more dielectric losses. These issues introduce significant complexity and diminish the reliability of the IMPA fabrication process. The development of reliable and efficient IMPAs, particularly those compatible with superconducting qubit fabrication processes, continues to be a focus of research.

In this Letter, we introduce the merged-element technique to design and fabricate the so-called merged-element JPA (MEJPA). In our design, the self-capacitance inherent in the Josephson junctions replaces the discrete parallel capacitor, effectively merging the superconducting quantum interference device (SQUID) and the parallel capacitor into a single integrated element. Compared to the traditional IMPA designs, our approach streamlines the fabrication process by obviating the need for discrete parallel capacitors. Typical IMPAs require a SQUID with a critical current of several microamperes ( $\mu$ As) and a discrete capacitor with a capacitance of several picofarads (pFs). In order to simultaneously meet the requirements for critical current and capacitance, Josephson junctions with junction areas on the order of tens of square micrometers were fabricated using the overlap method<sup>35</sup>. Owing to the concomitant influence of the Josephson junction oxidation layer on both critical current and junction capacitance, precise control of the oxidation parameters in the fabrication process is required. With the fabricated MEJPA, we achieved a gain of 15 dB (with 500 MHz bandwidth) and 10 dB (with 1 GHz bandwidth), operating near the quantum noise limit. Compared with the separate capacitor designs, merging the parallel capacitor into the Josephson junctions eliminates the shortcomings of conventional capacitors, makes the fabrica-

<sup>a)</sup>qu\_syt@163.com

<sup>b)</sup>jiezha@nju.edu.cn

tion process fully compatible with standard superconducting qubit production procedures, and also streamlines the fabrication process. Furthermore, the use of large-area Josephson junctions circumvents the need for high-precision exposure tools, such as electron beam lithography (EBL), throughout the fabrication process.

Figure 1(a) shows the layout of an impedance-transformed MEJPA device. An impedance transformer is comprised of a series-connected  $\lambda/4$  coplanar waveguide (CPW) resonator with characteristic impedance  $Z_{\lambda/4}$  (the orange part) and a  $\lambda/2$  coplanar waveguide (CPW) resonator with characteristic impedance  $Z_{\lambda/2}$  (the cyan part). These two resonators are designed to operate at the same resonant frequency  $\omega_i$ . This impedance transformer is coupled to the MEJPA, enabling the effective impedance matching and optimizing the bandwidth performance. These two resonators are designed to operate at the same resonant frequency  $\omega_i = 6.5$  GHz and are connected to the MEJPA, thereby enabling effective impedance matching and optimizing the bandwidth performance. The physical lengths of the  $\lambda/4$  and  $\lambda/2$  CPW sections on a sapphire substrate are approximately 4600 and 9200  $\mu\text{m}$ , respectively. The left end of the  $\lambda/4$  resonator is wire-bonded to the sample box, and then connected to a circulator in the measurement setup via a short microwave cable, as shown in Fig. 1(c). The right end of the  $\lambda/2$  section is terminated by the MEJPA, which contains a flux-pumped DC SQUID. In our design, the shunt capacitor is merged into the SQUID, making the MEJPA appear as a DC SQUID. A detailed view of the DC SQUID and its flux-pump line is shown in Fig. 1(b). Figure 1(c) illustrates the circuit diagram of the test setup for our device. The input signal goes through a circulator and is coupled to the MEJPA via an impedance transformer. The input impedance seen by the MEJPA is  $Z_{\text{in}}[\omega]$ ,

$$Z_{\text{in}}[\omega] = R + i\alpha\omega, \quad (1)$$

$$\alpha = 2Z_{\text{eff}}/\omega_i. \quad (2)$$

Here,  $Z_{\text{eff}}$  is the effective impedance of the impedance transformer, and the imaginary part  $\alpha$  can be tuned by the impedance transformer.<sup>23,36,37</sup> The input impedance  $Z_{\text{in}}[\omega]$  determines the reflection coefficient and thus the gain profile of the broadband parametric amplifier. The gain profile can be obtained by

$$G[\omega] = G_0 + G_2\omega^2 + G_4\omega^4 + \dots \quad (3)$$

Eliminating the quadratic coefficient  $G_2$  by adjusting  $\alpha$  enhances the gain-bandwidth product. The resulting bandwidth, determined by the oscillator linewidth  $\kappa_0$ , is given by

$$\Gamma_{\text{BW}} = \frac{\kappa_0}{2} \left( \frac{1}{G_0} \right)^{1/4}. \quad (4)$$

Typically, a DC SQUID primarily functions as a nonlinear inductor. In the MEJPA, the nonlinear inductor in conjunction with the inherent capacitance of the DC SQUID constitutes a lumped nonlinear oscillator. Therefore, the DC SQUID in our device performs the same function as a JPA with a discrete parallel capacitor. The equivalent circuit models of the DC

SQUID is shown in Fig. 1(d). The intrinsic capacitance of the Josephson junctions  $C_{J1}$  and  $C_{J2}$  functions as the parallel capacitor, forming  $C_{\text{SQUID}} = C_{J1} + C_{J2}$ . The equivalent circuit diagram reveals that the DC SQUID in our design is electrically equivalent to a parallel combination of a traditional DC SQUID and a discrete capacitor. The DC bias and the pump tone are combined using a bias tee and subsequently applied to the flux-pump line. The layout of the low-temperature measurement and control circuitry within the dilution refrigerator is presented in the supplementary material.

The circuit of our device is generally consisted of two layers, the base layer and the merged-element Josephson junction (MEJJ) layer. To fabricate the desired circuit, we first deposit a 100 nm aluminum film on a 2-in c-plane sapphire substrate with an ultrahigh vacuum (UHV) e-beam evaporation system. The desired pattern for the first layer is generated by exposing positive photoresist MICROPOSIT S1813 on the deposited film with a Heidelberg DWL66+ laser lithography system. Then the wafer is developed in the tetramethyl ammonium hydroxide based developer at room temperature. After a wet etching process, we obtain the pattern of the base layer, which defines the impedance transformer circuit, the flux-pump line and the bottom layer of the merged-element Josephson junctions.

In order to obtain the MEJJ layer, we use the bottom undercut layer PMGI SF6 and upper layer MICROPOSIT S1813 to create a bilayer structure. The top electrode pattern of the Josephson junction is defined using a laser lithography system aligned to the base layer. Following the development process, the wafer is loaded into the UHV e-beam evaporation system. An *in-situ* argon-ion milling process is then employed to remove the native oxide on the bottom electrode of the overlap junctions. Subsequently, the bottom electrode is oxidized in a static oxygen atmosphere at 100-Torr for 1-h to achieve the desired  $\text{Al}_2\text{O}_3$  layer thickness. A 200 nm thick aluminum film is then deposited using an electron beam evaporation system. After liftoff, we obtain the overlap junctions. In our fabrication process, the oxidation conditions are crucial for determining the junction resistance and capacitance.

To obtain the appropriate MEJPA resonant frequency, we needed to identify the critical current of the SQUIDs. The critical current  $I_c$  is calculated using the Ambegaokar-Baratoff formula,  $I_c = \pi\Delta/2eR_n$ ,<sup>38</sup> where  $\Delta$  is the superconducting energy gap and  $R_n$  is the SQUID resistance measured at room temperature. We fabricated and tested the room temperature resistance of SQUIDs with varying junction areas  $A_{JJ}$  under oxidation conditions of 100-Torr for 1-h, as shown in Fig. 2(a). Considering the large-area nature of the overlap junctions, we tested two different argon-ion milling methods to improve the process stability. One method involved rotating the chip at 10 rpm during milling, while the other performed milling from four orthogonal directions. The error bars reflect the uniformity of junction resistance across the entire 2-inch chip. In this work, we chose the second milling method in the fabrication process. Based on the Ambegaokar-Baratoff relation and our resistance measurements, we estimate a typical critical current density of  $J_c \approx 40$  nA/ $\mu\text{m}^2$ . Combining the SQUID room-temperature resistance with the peak resonant

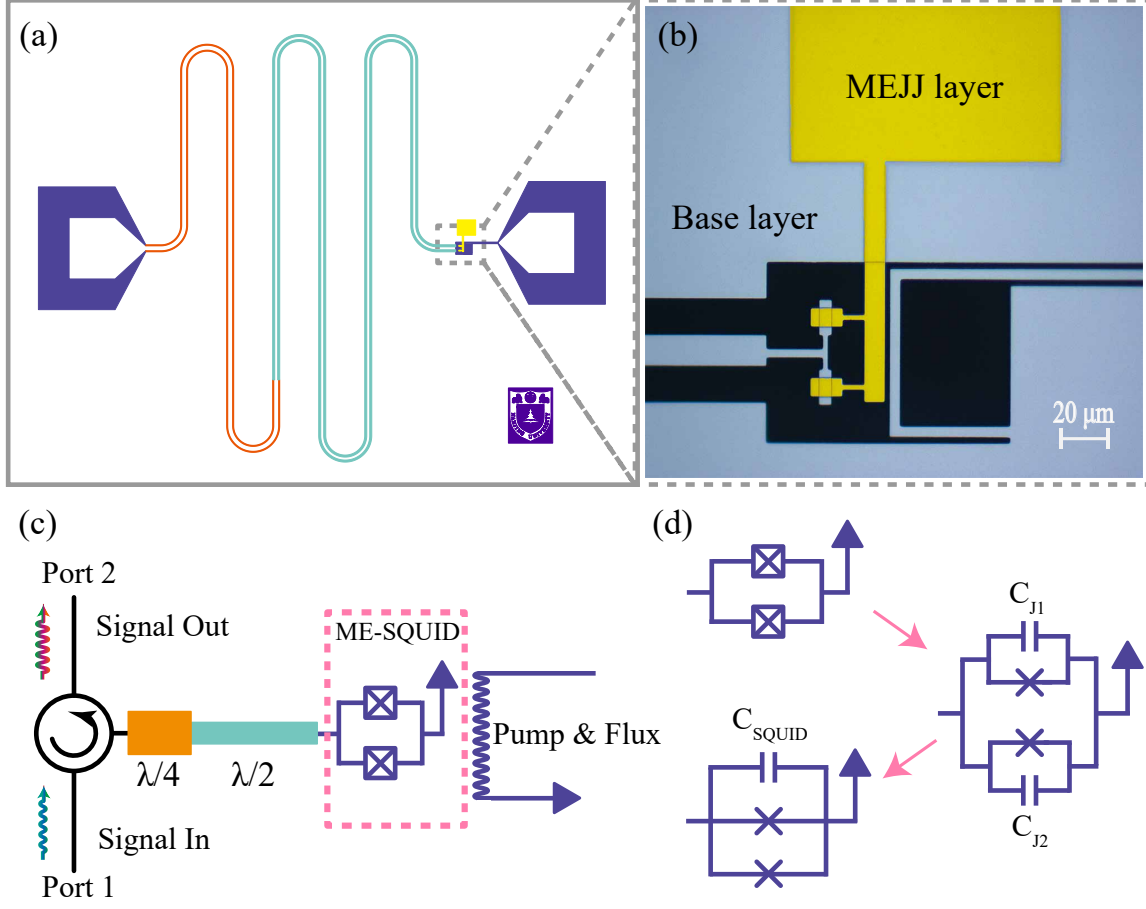


FIG. 1. (a) The layout of the merged-element broadband Josephson parametric amplifier. The CPW impedance transformer consists of a series-connected  $\lambda/4$  resonator (orange) and  $\lambda/2$  resonator (cyan), both designed to resonate at 6.5 GHz. (b) Optical micrograph of a zoomed-in view of the merged-element JPA. The entire chip consists of the base layer (dusty blue part) and the MEJJ layer (yellow part), which is highlighted in yellow false color. (c) The circuit diagram of our device. The left end of the  $\lambda/4$  resonator is wire-bonded to the sample box, and then connected to a circulator in the measurement setup via a short microwave cable. The right end of the  $\lambda/2$  resonator is terminated by the MEJPA device, which includes a flux-pumped DC SQUID connected to ground. (d) The equivalent models of the MEJPA, which is highlighted by the pink dashed box in (c).

frequency measured at low temperatures, we deduced the capacitance value  $C_{\text{SQUID}}$  using Eq. 5, as represented by the teal bars in Fig. 2(a). Based on the results, we can estimate the capacitance density of the SQUID is about  $38 \text{ fF}/\mu\text{m}^2$ . To provide quantitative insight into the junction parameters relevant to device performance, we fabricated MESQUIDs with varying junction areas and characterized their resistance and capacitance. The resistance-area product (RA) and the capacitance per unit area ( $C/A$ ) are plotted in Fig. 2(b). The RA values were directly obtained from room-temperature resistance measurements, while  $C/A$  values were deduced from the resonant frequencies of the corresponding nonlinear oscillators at low temperatures. The slight variation in RA values may in part originate from not accounting for the junction side-wall area in the defined junction size<sup>35</sup>. These results validate the consistency of our fabrication process and provide critical metrics for comparing junction uniformity and capacitance density. The specific design parameters of our parametric amplifier are detailed in Table I.

In our experiment, the device operates at three-wave mixing mode with a flux pump frequency of  $\omega_p \approx 2\omega_s$ . While our device can also operate as a four-wave mixing amplifier, three-wave mixing operation avoids frequency collisions and prevents saturation of the subsequent high-electron-mobility transistor (HEMT) amplifier due to excessive pump power. In the absence of pumping, we measured the transmission spectra  $S_{21}$  under different DC magnetic flux biases, as shown in Fig. 3. Due to the periodic flux dependence of the Josephson inductance in the SQUID, the resonant frequency exhibits a periodic variation with a period of one magnetic flux quantum  $\Phi_0$ . Figure 3 presents the resonance tuning over a single flux period, where the frequency varies from approximately 4 GHz to 9 GHz. The device demonstrates repeated operational windows due to this periodicity, and the flux bias point  $\Phi_{\text{DC}} = 0.334 \Phi_0$ , indicated by the black pentagram, was chosen for optimal performance in our gain and noise measurements. The black dashed line indicates the resonant frequency

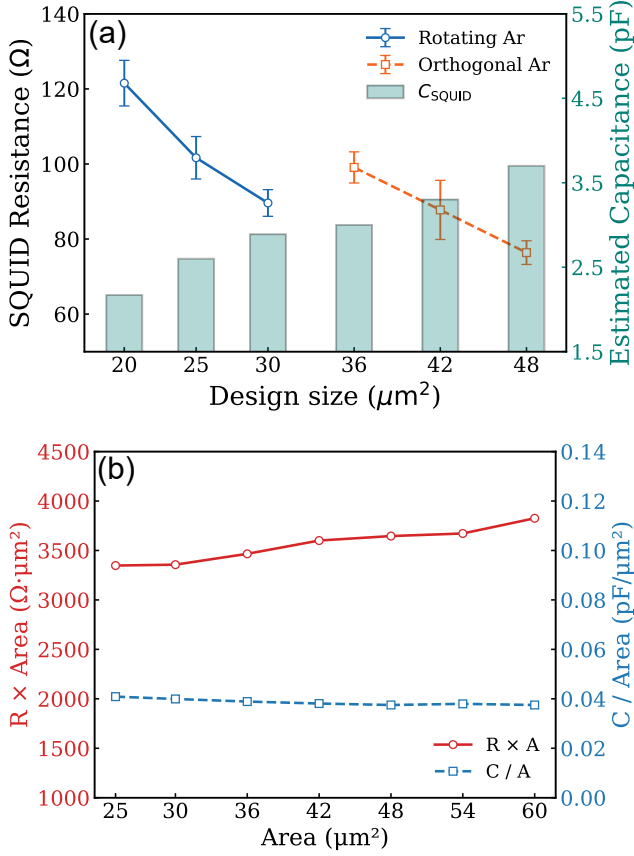


FIG. 2. (a) The measured Room-temperature resistance and capacitance of the SQUIDs for different junction areas. The x-axis represents the defined junction area of a single Josephson junction. The Josephson junctions are fabricated by oxidizing an aluminum film in 100 torr static oxygen for 1-h. The blue line corresponds to results obtained with chip rotation during argon-ion milling at 10 rpm, while the orange line represents results from continuous argon-ion milling at four orthogonal angles. The teal bars (histogram) show the capacitance estimated from low-temperature resonant frequency measurements. (b) Resistance-area product (RA, red circles) and capacitance per unit area (C/A, blue squares) for SQUIDs with different junction sizes. RA values are obtained from room-temperature resistance measurements. C/A values are extracted from low-temperature resonant frequency fitting.

$\omega_t$	$Z_{\lambda/4}$	$Z_{\lambda/2}$	$I_{\text{SQUID}}$	$C_{\text{SQUID}}$	$A_{\text{JJ}}$
6.5 GHz	38.5 Ω	65 Ω	3.8 μA	3.6 pF	48 μm <sup>2</sup>

TABLE I. The design parameters of MEJPA.

calculated by the following equation<sup>20</sup>:

$$\Omega_p(\Phi_{\text{DC}}) = \frac{1}{\sqrt{C_J(L_J/\cos(\pi\Phi_{\text{DC}}/\Phi_0) + L_s)}}. \quad (5)$$

Here,  $\Phi_{\text{DC}}$  is the dc bias magnetic flux penetrating the SQUID loop.  $\Phi_0$  is the flux quantum.  $C_J$  and  $L_J$  are the capacitance and the Josephson inductance of the SQUID, respectively.  $L_s$  is the stray inductance between the SQUID and the ground.

As the HEMT amplifier operates within the frequency range of 4-8 GHz, a significant deterioration in the signal-to-noise ratio is observed above 8 GHz in Figure. 3.

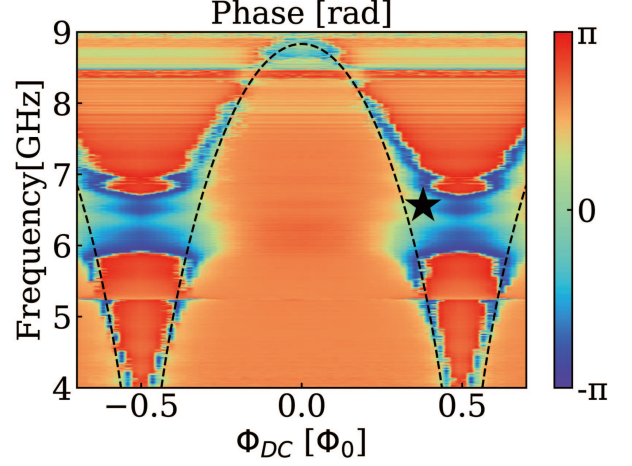


FIG. 3. Phases of the transmission spectra  $S_{21}$  as a function of DC flux  $\Phi_{\text{DC}}$  without pump. The resonant frequency of the nonlinear resonator can be tuned from 4 to approximately 9 GHz. Black dashed lines represent the calculated resonant frequencies. The black pentagram indicates the operating point, where  $\Phi_{\text{DC}} = 0.334 \Phi_0$ .

To characterize the amplification performance of our device, we optimized the operating point around 6.5 GHz. A flux pump with an on-chip power of  $P_{\text{pump}} \approx -53$  dBm and a frequency of  $f_{\text{pump}} = 13.04715$  GHz was applied to the flux-pump line. This on-chip value was determined by accounting for all cryogenic line attenuations and confirmed via calibration. Our calibration approach, combining standard two-port VNA measurements with independently measured cryogenic line losses, allowed accurate extraction of the intrinsic  $S_{21}$  response. In the course of this work, we became aware of a more systematic in-operando calibration methodology proposed for parametric amplifiers<sup>39</sup>, which may offer further improvements for future amplifier characterization. Under these conditions, an instantaneous gain exceeding 15 dB was achieved over a 500 MHz bandwidth, as shown in Fig. 4(a). Moreover, gain performance exceeding 10 dB was also achieved under other parameters, with the maximum bandwidth surpassing 1 GHz. (see the supplementary material for details). The ripple observed in the gain profile is attributed to the frequency-dependent impedance mismatch caused by standing waves in the input line, such as reflections from the circulator cable or bonding interfaces. These cause periodic variations in the input admittance seen by the amplifier, which in turn modulate the gain, as discussed in Ref.<sup>36</sup>. To qualitatively understand how key design parameters affect amplifier performance, we performed numerical simulations of gain profiles as functions of the MESQUID shunt capacitance and the characteristic impedances of the  $\lambda/2$  and  $\lambda/4$  transmission line sections. The details of these simulations are also provided in the supplementary material. The MEJPA's linear amplification range was characterized by measuring the 1 dB compression power across its gain bandwidth. By gradually increasing

the input signal power, we determined the 1 dB compression point, which corresponds to an average saturation power of approximately -116 dBm [Fig. 4(b)].

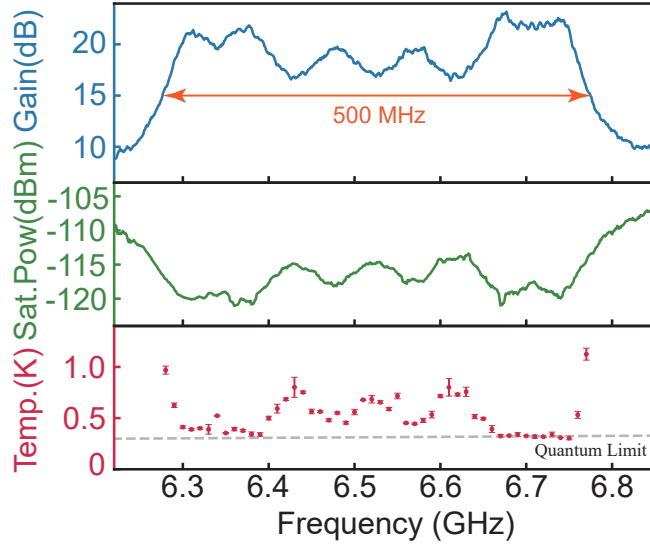


FIG. 4. The gain profile (a), saturation power (b), and noise performance (c) of the MEJPA. The operating point is indicated by the black pentagram marker in Fig. 3, with pump frequency  $f_{\text{pump}} = 13.04715$  GHz, pump power  $P_{\text{pump}} \approx -53$  dBm, and magnetic flux bias  $\Phi_{\text{DC}} = 0.334 \Phi_0$ . The ripple observed across the amplified band originates from standing waves caused by residual impedance mismatch in the measurement chain<sup>29,36</sup>.

In addition to gain and bandwidth, noise temperature is a crucial performance metric for parametric amplifiers. In this work, we determined the noise temperature  $T_{\text{JPA}}$  of the MEJPA using the  $\Delta\text{SNR}$  method,<sup>23,36,40</sup>

$$T_{\text{JPA}} = T_{\text{sys}} \left( \frac{1}{\Delta\text{SNR}} - \frac{1}{G_{\text{JPA}}} \right) + T_{\text{in}} \left( \frac{1}{\Delta\text{SNR}} - 1 \right), \quad (6)$$

$$T_{\text{sys}} = T_{\text{in}} + T_{\text{JPA}} + T_{\text{HEMT}}/G_{\text{JPA}}. \quad (7)$$

Here,  $T_{\text{HEMT}}$  is the HEMT noise calibrated by the Y-factor method,<sup>21,22,41</sup>  $\Delta\text{SNR}$  represents the improvement of signal-to-noise (SNR) between the pump on and off, and  $T_{\text{in}}$  is the input noise temperature, which is approximately equal to the vacuum noise temperature. The results presented in Fig. 4(c) demonstrate that the noise of our amplifier approaches the quantum limit.<sup>42,43</sup> The circuit diagram of the noise measurement setup can be found in the supplementary material.

In conclusion, we have presented a merged-element technique for designing and fabricating high-performance broadband Josephson parametric amplifiers. Our design eliminates the need for discrete capacitors, simplifying the fabrication process, reducing the requirements for high-precision exposure tools, and ensuring compatibility with standard superconducting qubit fabrication procedures. Furthermore, the increased oxidation layer thickness enhances the dielectric strength of the Josephson junctions, effectively mitigating the electrostatic failure risk of the MEJPA. According to the simulation results, the gain profile can be further optimized by

fine-tuning the impedance and control parameters. Our results demonstrate a promising Josephson parametric amplifier suitable for multi-qubit measurement architectures and with broader implications for quantum information processing.

See the supplementary material for detailed descriptions of the experimental setup, additional gain-bandwidth results, numerical simulations illustrating design parameter dependencies, and performance benchmarking of the MEJPA against other IMPAs utilizing discrete capacitor implementations.

This work was partly supported by the Innovation Program for Quantum Science and Technology (2021ZD0301702), the National Natural Science Foundation of China (NSFC) (U21A20436, 12074179 and 12205147), the Natural Science Foundation of Jiangsu Province, China (Grant Nos. BE2021015-1 and BK20232002), the Natural Science Foundation of Shan-dong Province (Grant No. ZR2023LZH002).

## DATA AVAILABILITY

The data that support the findings of this study are available from the corresponding author upon reasonable request.

## REFERENCES

- <sup>1</sup>E. Jeffrey, D. Sank, J. Y. Mutus, T. C. White, J. Kelly, R. Barends, Y. Chen, Z. Chen, B. Chiaro, A. Dunsworth, A. Megrant, P. J. J. O'Malley, C. Neill, P. Roushan, A. Vainsencher, J. Wenner, A. N. Cleland, and J. M. Martinis, "Fast accurate state measurement with superconducting qubits," *Phys. Rev. Lett.* **112**, 190504 (2014).
- <sup>2</sup>T. Joas, A. M. Waeber, G. Braunbeck, and F. Reinhard, "Quantum sensing of weak radio-frequency signals by pulsed mollow absorption spectroscopy," *Nature Communications* **8**, 964 (2017).
- <sup>3</sup>Z. Wang, M. Xu, X. Han, W. Fu, S. Puri, S. M. Girvin, H. X. Tang, S. Shankar, and M. H. Devoret, "Quantum microwave radiometry with a superconducting qubit," *Phys. Rev. Lett.* **126**, 180501 (2021).
- <sup>4</sup>C. Braggio, G. Carugno, F. Della Valle, G. Galeazzi, A. Lombardi, G. Russo, and D. Zanello, "The measurement of a single-mode thermal field with a microwave cavity parametric amplifier," *New Journal of Physics* **15**, 013044 (2013).
- <sup>5</sup>M. A. Castellanos-Beltran and K. W. Lehnert, "Widely tunable parametric amplifier based on a superconducting quantum interference device array resonator," *Applied Physics Letters* **91**, 083509 (2007).
- <sup>6</sup>T. Yamamoto, K. Inomata, M. Watanabe, K. Matsuba, T. Miyazaki, W. D. Oliver, Y. Nakamura, and J. S. Tsai, "Flux-driven Josephson parametric amplifier," *Applied Physics Letters* **93**, 042510 (2008).
- <sup>7</sup>J. Aumentado, "Superconducting Parametric Amplifiers: The State of the Art in Josephson Parametric Amplifiers," *IEEE Microwave Magazine* **21**, 45–59 (2020).
- <sup>8</sup>F. Mallet, F. R. Ong, A. Palacios-Laloy, F. Nguyen, P. Bertet, D. Vion, and D. Esteve, "Single-shot qubit readout in circuit quantum electrodynamics," *Nature Physics* **5**, 791–795 (2009).
- <sup>9</sup>Z. Lin, K. Inomata, W. Oliver, K. Koshino, Y. Nakamura, J. Tsai, and T. Yamamoto, "Single-shot readout of a superconducting flux qubit with a flux-driven Josephson parametric amplifier," *Applied Physics Letters* **103** (2013).
- <sup>10</sup>F. Mallet, M. A. Castellanos-Beltran, H. S. Ku, S. Glancy, E. Knill, K. D. Irwin, G. C. Hilton, L. R. Vale, and K. W. Lehnert, "Quantum state tomography of an itinerant squeezed microwave field," *Phys. Rev. Lett.* **106**, 220502 (2011).
- <sup>11</sup>C. Eichler, D. Bozyigit, C. Lang, M. Baur, L. Steffen, J. M. Fink, S. Filipp, and A. Wallraff, "Observation of two-mode squeezing in the microwave frequency domain," *Phys. Rev. Lett.* **107**, 113601 (2011).

- <sup>12</sup>M. Hatridge, S. Shankar, M. Mirrahimi, F. Schackert, K. Geerlings, T. Brecht, K. M. Sliwa, B. Abdo, L. Frunzio, S. M. Girvin, R. J. Schoelkopf, and M. H. Devoret, “Quantum back-action of an individual variable-strength measurement,” *Science* **339**, 178–181 (2013).
- <sup>13</sup>K. W. Murch, S. Weber, C. Macklin, and I. Siddiqi, “Observing single quantum trajectories of a superconducting quantum bit,” *Nature* **502**, 211–214 (2013).
- <sup>14</sup>S. Weber, A. Chantasri, J. Dressel, A. N. Jordan, K. W. Murch, and I. Siddiqi, “Mapping the optimal route between two quantum states,” *Nature* **511**, 570–573 (2014).
- <sup>15</sup>R. Vijay, C. Macklin, D. Slichter, S. Weber, K. Murch, R. Naik, A. N. Korotkov, and I. Siddiqi, “Stabilizing rabi oscillations in a superconducting qubit using quantum feedback,” *Nature* **490**, 77–80 (2012).
- <sup>16</sup>J. F. Marques, B. Varbanov, M. Moreira, H. Ali, N. Muthusubramanian, C. Zachariadis, F. Battistel, M. Beekman, N. Haider, W. Vlothuizen, et al., “Logical-qubit operations in an error-detecting surface code,” *Nature Physics* **18**, 80–86 (2022).
- <sup>17</sup>S. Krinner, N. Lacroix, A. Remm, A. Di Paolo, E. Genois, C. Leroux, C. Hellings, S. Lazar, F. Swiadek, J. Herrmann, et al., “Realizing repeated quantum error correction in a distance-three surface code,” *Nature* **605**, 669–674 (2022).
- <sup>18</sup>V. Sivak, A. Eickbusch, B. Royer, S. Singh, I. Tsioutsios, S. Ganjam, A. Milano, B. Brock, A. Ding, L. Frunzio, et al., “Real-time quantum error correction beyond break-even,” *Nature* **616**, 50–55 (2023).
- <sup>19</sup>M. Hatridge, R. Vijay, D. H. Slichter, J. Clarke, and I. Siddiqi, “Dispersive magnetometry with a quantum limited SQUID parametric amplifier,” *Physical Review B* **83**, 134501 (2011).
- <sup>20</sup>J. Y. Mutus, T. C. White, E. Jeffrey, D. Sank, R. Barends, J. Bochmann, Y. Chen, Z. Chen, B. Chiaro, A. Dunsworth, J. Kelly, A. Megrant, C. Neill, P. J. J. O’Malley, P. Roushan, A. Vainsencher, J. Wenner, I. Siddiqi, R. Vijay, A. N. Cleland, and J. M. Martinis, “Design and characterization of a lumped element single-ended superconducting microwave parametric amplifier with on-chip flux bias line,” *Applied Physics Letters* **103**, 122602 (2013).
- <sup>21</sup>J. Y. Mutus, T. C. White, R. Barends, Y. Chen, Z. Chen, B. Chiaro, A. Dunsworth, E. Jeffrey, J. Kelly, A. Megrant, C. Neill, P. J. J. O’Malley, P. Roushan, D. Sank, A. Vainsencher, J. Wenner, K. M. Sundqvist, A. N. Cleland, and J. M. Martinis, “Strong environmental coupling in a Josephson parametric amplifier,” *Applied Physics Letters* **104**, 263513 (2014).
- <sup>22</sup>T. Elo, T. S. Abhilash, M. R. Perelshtein, I. Lilja, E. V. Korostylev, and P. J. Hakonen, “Broadband lumped-element Josephson parametric amplifier with single-step lithography,” *Applied Physics Letters* **114**, 152601 (2019).
- <sup>23</sup>P. Duan, Z. Jia, C. Zhang, L. Du, H. Tao, X. Yang, L. Guo, Y. Chen, H. Zhang, Z. Peng, W. Kong, H.-O. Li, G. Cao, and G.-P. Guo, “Broadband flux-pumped Josephson parametric amplifier with an on-chip coplanar waveguide impedance transformer,” *Applied Physics Express* **14**, 042011 (2021).
- <sup>24</sup>J. Grebel, A. Bienfait, É. Dumur, H.-S. Chang, M.-H. Chou, C. R. Conner, G. A. Peairs, R. G. Povey, Y. P. Zhong, and A. N. Cleland, “Flux-pumped impedance-engineered broadband Josephson parametric amplifier,” *Applied Physics Letters* **118**, 142601 (2021).
- <sup>25</sup>Y. Lu, W. Xu, Q. Zuo, J. Pan, X. Wei, J. Jiang, Z. Li, K. Zhang, T. Guo, S. Wang, C. Cao, H. Wang, W. Xu, G. Sun, and P. Wu, “Broadband Josephson parametric amplifier using lumped-element transmission line impedance matching architecture,” *Applied Physics Letters* **120**, 082601 (2022).
- <sup>26</sup>S. Wu, D. Zhang, R. Wang, Y. Liu, S.-P. Wang, Q. Liu, J. S. Tsai, and T. Li, “Vacuum-gap-based lumped element Josephson parametric amplifier,” *Chinese Physics B* **31**, 010306 (2022).
- <sup>27</sup>T. White, A. Opremcak, G. Sterling, A. Korotkov, D. Sank, R. Acharya, M. Ansmann, F. Arute, K. Arya, J. C. Bardin, et al., “Readout of a quantum processor with high dynamic range josephson parametric amplifiers,” *Applied Physics Letters* **122** (2023).
- <sup>28</sup>B. Qing, L. B. Nguyen, X. Liu, H. Ren, W. P. Livingston, N. Goss, A. Hajr, T. Chistolini, Z. Pedramrazi, D. I. Santiago, J. Luo, and I. Siddiqi, “Broadband coplanar-waveguide-based impedance-transformed josephson parametric amplifier,” *Phys. Rev. Res.* **6**, L012035 (2024).
- <sup>29</sup>T. Zhou, W. Xu, Q. Zuo, J. Pan, Z. Li, K. Zhang, T. Guo, Y. Sheng, L. Jing, H. Ma, et al., “Impedance matched josephson parametric amplifier with a multisection  $\lambda/4$  transmission line transformer,” *Applied Physics Letters* **126** (2025).
- <sup>30</sup>C. Macklin, K. O’Brien, D. Hover, M. E. Schwartz, V. Bolkhovskiy, X. Zhang, W. D. Oliver, and I. Siddiqi, “A near-quantum-limited Josephson traveling-wave parametric amplifier,” *Science* **350**, 307–310 (2015).
- <sup>31</sup>K. O’Brien, C. Macklin, I. Siddiqi, and X. Zhang, “Resonant Phase Matching of Josephson Junction Traveling Wave Parametric Amplifiers,” *Physical Review Letters* **113**, 157001 (2014).
- <sup>32</sup>C. Bockstiegel, J. Gao, M. R. Vissers, M. Sandberg, S. Chaudhuri, A. Sanders, L. R. Vale, K. D. Irwin, and D. P. Pappas, “Development of a Broadband NbTiN Traveling Wave Parametric Amplifier for MKID Readout,” *Journal of Low Temperature Physics* **176**, 476–482 (2014).
- <sup>33</sup>B. Ho Eom, P. K. Day, H. G. LeDuc, and J. Zmuidzinas, “A wideband, low-noise superconducting amplifier with high dynamic range,” *Nature Physics* **8**, 623–627 (2012).
- <sup>34</sup>M. Esposito, A. Ranadive, L. Planat, and N. Roch, “Perspective on traveling wave microwave parametric amplifiers,” *Applied Physics Letters* **119**, 120501 (2021).
- <sup>35</sup>M. Bal, J. Long, R. Zhao, H. Wang, S. Park, C. R. H. McRae, T. Zhao, R. E. Lake, V. Monarkha, S. Simbierowicz, D. Frolov, R. Pilipenko, S. Zorzetti, A. Romanenko, C.-H. Liu, R. McDermott, and D. P. Pappas, “Overlap junctions for superconducting quantum electronics and amplifiers,” *Applied Physics Letters* **118**, 112601 (2021).
- <sup>36</sup>T. Roy, S. Kundu, M. Chand, A. M. Vadiraj, A. Ranadive, N. Nehra, M. P. Patankar, J. Aumentado, A. A. Clerk, and R. Vijay, “Broadband parametric amplification with impedance engineering: Beyond the gain-bandwidth product,” *Applied Physics Letters* **107**, 262601 (2015).
- <sup>37</sup>O. Naaman and J. Aumentado, “Synthesis of parametrically coupled networks,” *PRX Quantum* **3**, 020201 (2022).
- <sup>38</sup>V. Ambegaokar and A. Baratoff, “Tunneling Between Superconductors,” *Phys. Rev. Lett.* **10**, 486–489 (1963).
- <sup>39</sup>S.-H. Shin, M. Stanley, W. Wong, T. Sweetnam, A. Elarabi, T. Lindström, N. Ridler, and S. de Graaf, “In-operando microwave scattering-parameter calibrated measurement of a josephson traveling wave parametric amplifier,” *Applied Physics Letters* **125** (2024).
- <sup>40</sup>M. Simoen, C. W. S. Chang, P. Krantz, J. Bylander, W. Wustmann, V. Shumeiko, P. Delsing, and C. M. Wilson, “Characterization of a multimode coplanar waveguide parametric amplifier,” *Journal of Applied Physics* **118**, 154501 (2015).
- <sup>41</sup>D. Pozar, *Microwave Engineering*, 4th ed. (Wiley, 2011).
- <sup>42</sup>C. M. Caves, “Quantum limits on noise in linear amplifiers,” *Physical Review D* **26**, 1817–1839 (1982).
- <sup>43</sup>A. A. Clerk, M. H. Devoret, S. M. Girvin, F. Marquardt, and R. J. Schoelkopf, “Introduction to quantum noise, measurement, and amplification,” *Rev. Mod. Phys.* **82**, 1155–1208 (2010).





losses at each temperature stage. This allowed accurate estimation of the on-chip signal and pump power.

To measure the amplifier noise, an input signal is generated by a microwave source and received by a spectrum analyzer with the pump both on and off. The system noise of the output line was characterized using the Y-factor method, which employed a cryogenic microwave switch to alternate between a 50-ohm termination at the still plate (acting as the hot source) and the MC stage (acting as the cold source).

### OTHER RESULTS OF MEJPA

In the low-temperature characterization, we also measured the amplifier bandwidth corresponding to a 10 dB gain under varying magnetic flux bias conditions. As shown in Fig. S2, the bandwidth exceeding 10 dB reached up to 1 GHz. However, the gain flatness remains suboptimal and could be further improved through enhanced impedance matching.

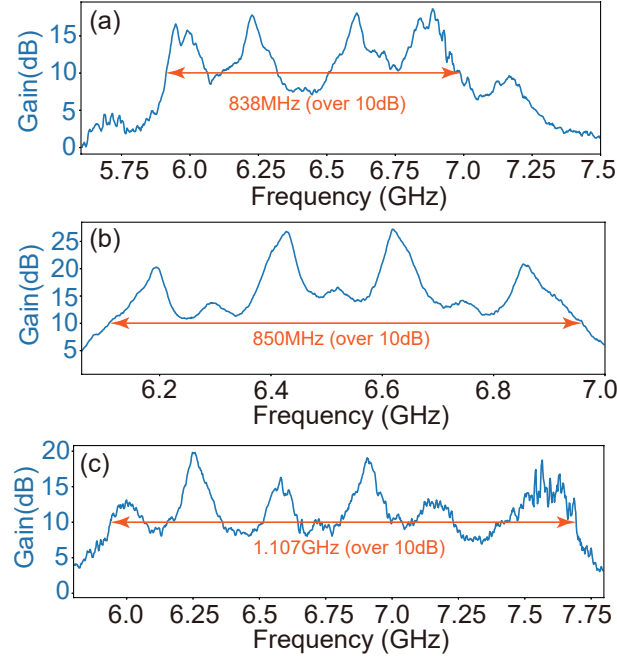


FIG. S2: The 10 dB gain profiles (a)(b)(c) of different devices are shown, with the orange line indicating the bandwidth where the gain exceeds 10 dB.

### NUMERICAL SIMULATIONS OF DESIGN PARAMETER DEPENDENCIES

To illustrate how key structural parameters in the MEJPA design influence amplifier performance, we performed numerical simulations based on a nonlinear resonator model comprising a Josephson junction and embedded transmission lines [1]. The gain response was calculated under variations of three critical parameters.

Figure S3(a) shows the dependence of gain bandwidth and peak gain on the MESQUID shunt capacitance  $C_s$ , which is integrated directly into the SQUID structure. Figures S3(b) and (c) present the effects of the characteristic impedances  $Z_{\lambda/2}$  and  $Z_{\lambda/4}$  of the half- and quarter-wavelength coplanar waveguide sections, respectively. These two sections together control the impedance transformation and influence the peak gain, ripple behavior, and bandwidth matching.

These simulation results provide guidance for optimizing design parameters to achieve broadband and flat gain performance in merged-element architectures.



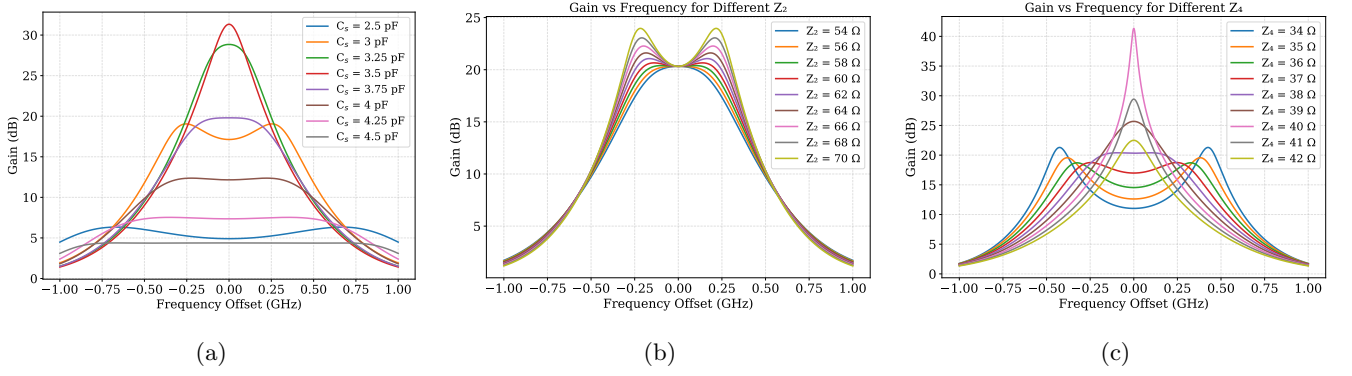


FIG. S3: Simulated gain profiles showing dependence on key structural parameters: (a) MESQUID shunt capacitance  $C_s$ ; (b) Characteristic impedance  $Z_{\lambda/2}$  of the half-wavelength section; (c) Characteristic impedance  $Z_{\lambda/4}$  of the quarter-wavelength matching section.

### IMPA PERFORMANCE COMPARISON WITH DIFFERENT CAPACITOR DESIGNS

To highlight the advantages of merging the shunting capacitor into the SQUID structure, and coupling it via the impedance transformer. We compare our MEJPA design with prior broadband JPAs that employ separate lumped capacitors. Table S1 summarizes key performance parameters, including gain, bandwidth, saturation power, on-chip pump power, and qualitative fabrication complexity.

TABLE S1: Benchmarking of the MEJPA against other broadband JPAs.

Device	Gain (dB)	BW (MHz)	$P_{\text{1dB}}$ (dBm)	Pump Power (dBm)	Fabrication Complexity
<b>This work (MEJPA)</b>	15	500	-116	-53	<b>Low</b> (merged capacitor)
Duan et al. (2021)[2]	15	600	-110	-55 <sup>†</sup>	Moderate (separate dielectric $C_p$ )
Wu et al. (2022)[3]	20	162	-123	—	High (vacuum-gap-based $C_p$ )

<sup>†</sup>Estimated from on-chip attenuation and pump line loss, based on supplementary information. The third row does not report on-chip pump power.

Compared to parametric amplifier designs with discrete capacitors, the MEJPA integrates the capacitive element directly into the SQUID structure, eliminating the need for separate capacitor components. This merged-element configuration significantly reduces parasitic inductance, improves impedance matching, and simplifies the fabrication process.

### REFERENCES

- \* qu\_syt@163.com  
<sup>†</sup> jiezhao@nju.edu.cn
- [1] T. Roy, S. Kundu, M. Chand, A. M. Vadiraj, A. Ranadive, N. Nehra, M. P. Patankar, J. Aumentado, A. A. Clerk, and R. Vijay, Applied Physics Letters **107**, 262601 (2015), ISSN 0003-6951, 1077-3118, URL <https://pubs.aip.org/apl/article/107/26/262601/235920/Broadband-parametric-amplification-with-impedance>.
  - [2] P. Duan, Z. Jia, C. Zhang, L. Du, H. Tao, X. Yang, L. Guo, Y. Chen, H. Zhang, Z. Peng, et al., Applied Physics Express **14**, 042011 (2021), ISSN 1882-0778, 1882-0786, URL <https://iopscience.iop.org/article/10.35848/1882-0786/abf029>.
  - [3] S. Wu, D. Zhang, R. Wang, Y. Liu, S.-P. Wang, Q. Liu, J. S. Tsai, and T. Li, Chinese Physics B **31**, 010306 (2022), ISSN 1674-1056, URL <https://iopscience.iop.org/article/10.1088/1674-1056/ac280c>.